

A Single-Chip Electron Paramagnetic Resonance Transceiver in 0.13- μm SiGe BiCMOS

Xuebei Yang, *Student Member, IEEE*, and Aydin Babakhani, *Member, IEEE*

Abstract—We report the first absorption-based single-chip transceiver for electron paramagnetic resonance (EPR) spectroscopy in silicon. The chip is implemented in a 0.13- μm SiGe BiCMOS process technology. The transmitter generates and delivers a continuous-wave microwave signal with a frequency range from 895 to 979 MHz and the receiver adopts a direct-conversion architecture. Based on the single-chip transceiver and a printed-circuit-board-based planar resonator, an EPR spectrometer is assembled and tested. The spectrometer successfully measures the EPR response from samples including 2,2-Diphenyl-1-Picrylhydrazyl powder, Fe_3O_4 nanoparticles, and Fe_2O_3 nanoparticles.

Index Terms—BiCMOS, CMOS, electron paramagnetic resonance (EPR), electron spin resonance (ESR), SiGe, silicon, single-chip, transceiver.

I. INTRODUCTION

ELECTRON paramagnetic resonance (EPR) or electron spin resonance (ESR) phenomenon is based on the interaction of electromagnetic radiation with an electron magnetic dipole moment in the presence of a dc magnetic field [1]. It is in concept similar to nuclear magnetic resonance (NMR). However, in NMR, the magnetic moments that interact with electromagnetic radiation result from nuclei such as ^1H and ^{13}C [2], while in EPR the magnetic moments arise from unpaired electrons [1]–[3]. Due to the larger magnetic moment of electrons compared to nuclei (660 times larger compared to ^1H), the signal intensity per spin of EPR is considerably higher than that of NMR, giving EPR a distinct advantage over NMR in sensitivity per spin. The first observation of EPR was made in 1945 by Zavoisky, who detected an RF absorption line from a $\text{CuCl}_2 \cdot 2\text{H}_2\text{O}$ sample [1]. Since then, EPR spectroscopy has found its application in numerous fields. In clinical medicine, EPR spectroscopy provides the only approach for the direct and noninvasive measurement of partial oxygen pressure (pO_2), which is critical for the ionizing radiation therapy of cancer and successful healing of wounds [4]–[6]. In material science, EPR spectroscopy has long been used to characterize the point defects in semiconductor lattice, including silicon, silicon

carbide, zinc oxide, etc. [7]–[9]. In chemistry studies, EPR spectroscopy is a powerful tool to study the magnetic properties of high-nuclearity transition-metal complexes [10].

While EPR spectroscopy has demonstrated its value in various fields, this technique is only exploited in a few number of research laboratories. There is hardly any utilization of EPR spectroscopy for in-field or *in vivo* applications. This situation is not due to the lack of demand for EPR spectroscopy outside laboratories. For example, it is reported that *in vivo* EPR is a promising and valuable addition to clinical medicine [11]. It could be used to monitor the response of cancer treatment. However, there are major deficiencies in existing EPR spectrometers that limit their applications. Currently, most EPR spectrometers are composed of three major components: a magnet, a resonator, and an electrical transceiver [3]. The electrical transceiver, in its current form, is mostly made up of a large number of discrete circuits built from dedicated and expensive components. As a result, the cost and size of the existing EPR spectrometers are prohibitively large, restricting the employment of the spectrometers in various fields or *in vivo* applications. In the past few years, several groups reported integration of EPR electronics. However, the level of integration is still low and insufficient at this moment [12], [13]. Moreover, in the prior work, samples had to be precisely placed onto an on-chip inductor, whose diameter is no larger than 300 μm . This significantly increases the difficulty of measurement.

Given the deficiencies of existing EPR spectrometers, we propose to integrate the entire EPR transceiver on a single silicon chip. Therefore, the cost, weight, and physical size of the EPR spectrometer can be significantly reduced. In order to demonstrate the feasibility of the proposed EPR spectrometer, in this work, we have designed a fully integrated transceiver chip in IBM 0.13- μm SiGe BiCMOS process technology. An EPR spectrometer is then assembled using the transceiver chip and a printed circuit board (PCB)-based planar resonator fabricated in-house. Utilizing the proposed EPR spectrometer, measurements of various samples, including 2,2-Diphenyl-1-Picrylhydrazyl (DPPH) powder, Fe_3O_4 nanoparticles, and Fe_2O_3 nanoparticles, have been successfully performed at room temperature. The observed EPR spectrum from these samples is consistent with previously published results, demonstrating the functionality of the proposed EPR spectrometer. This work was briefly and previously reported in [14]. It will be presented in more detail in this paper, including more theoretical background on EPR, circuit details, and measurement results.

This paper is outlined as follows. Section II presents the physical mechanism of EPR. Section III introduces the architecture

Manuscript received November 30, 2014; revised April 12, 2015, June 07, 2015, and September 09, 2015; accepted September 16, 2015. Date of publication October 06, 2015; date of current version November 03, 2015.

The authors are with the Electrical and Computer Engineering Department, Rice University, Houston, TX 77005 USA (e-mail: xbyang@rice.edu; aydin.babakhani@rice.edu).

Color versions of one or more of the figures in this paper are available online at <http://ieeexplore.ieee.org>.

Digital Object Identifier 10.1109/TMTT.2015.2481895

of the proposed EPR spectrometer and discusses the design considerations. In Section IV, the circuit details of a fully integrated transceiver is discussed. The design of the PCB-based planar resonator is described in Section V. The measurement results of the transceiver and spectrometer are shown in Section VI. This paper is concluded in Section VII.

II. BACKGROUND

This section describes the physical principles of the EPR phenomenon. A complete review of EPR would require a comprehensive treatment using quantum mechanics, which is outside the scope of this paper. Therefore, a semi-classical approach is adopted to present the basic concepts of EPR.

We begin by considering a magnetic dipole of moment $\vec{\mu}$ in a static magnetic field \vec{B}_0 . Assuming the magnetic field \vec{B}_0 is taken along the \vec{z} direction, the magnetic dipole preserves an energy level U ,

$$U = -\vec{\mu} \cdot \vec{B}_0 = -\mu B_0 \cos(\angle \vec{\mu} \vec{B}_0) = -\mu_z B_0. \quad (1)$$

Here, μ_z is the component of $\vec{\mu}$ along the \vec{z} direction. It is observed that for a given value of B_0 , there exists a minimum energy $-\mu B_0$, corresponding to the situation where the angle between $\vec{\mu}$ and \vec{B}_0 is 0° . There is also a maximum energy μB_0 , corresponding to the case where the angle between $\vec{\mu}$ and \vec{B}_0 is 180° .

Next, we consider the magnetic moment generated from an electron. From classical physics, since the electron is a charged particle, it generates a current loop when it rotates around a nucleus. This current loop generates a magnetic moment as given by the following equation:

$$\mu_z = \alpha g \beta M_s. \quad (2)$$

Here, $\alpha = -1$ for an electron. g is known as the g factor. It is equal to 2.002319304386 for free electrons [1]. For electrons where interaction with other particles exists, g is usually different from this value. M_s is the secondary spin quantum number. For a system with spin number s , M_s ranges from $-s$ to $+s$ with steps of 1. This generates $2s + 1$ possible values of M_s . β is the *Bohr magneton*. It is evaluated as $\beta = (e\hbar)/(2m) = 9.2740154 \times 10^{-24} \text{ JT}^{-1}$ [1]. Here, e is the charge of an electron, \hbar is the Planck's constant, and m is the mass of an electron.

If an electron is placed inside a static magnetic field B_0 , according to (1) and substituting μ_z using (2), the electron would have a set of possible energy levels $U = g\beta B_0 M_s$. For a spin 1/2 system, where the possible values of M_s are $+1/2$ and $-1/2$, there are two possible energy states. $U_{\text{upper}} = (1)/(2)g\beta B_0$, $U_{\text{lower}} = -(1/2)g\beta B_0$, and $\Delta U = U_{\text{upper}} - U_{\text{lower}} = g\beta B_0$, as shown in Fig. 1. In an atomic system, the Pauli exclusion principle illustrates that no more than two electrons can occupy a given orbital. When two electrons occupy any given orbital, their secondary spin quantum numbers M_s have to be different. Therefore, both energy states U_{upper} and U_{lower} will be occupied and an electron transition cannot happen. On the other hand, if an orbital in a chemical species contains only one electron (unpaired electron), one

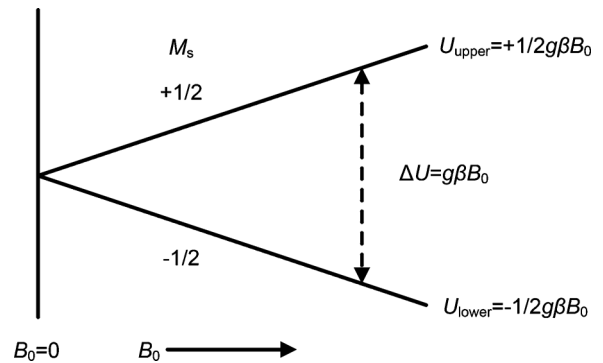


Fig. 1. Splitting of energy levels of electrons in a spin 1/2 system.

energy state will be vacant and the electron energy transition is possible.

For those chemical species with unpaired electrons, an electron transition from U_{lower} to U_{upper} may be induced by an electromagnetic field B_1 with appropriate frequency ω such that the photon energy satisfies

$$\hbar\omega = \Delta U = g\beta B_0. \quad (3)$$

The frequency ω typically falls into the microwave regime. Besides the criteria shown in (3), the transition also poses a requirement for the angular momentum of the incoming photon. A detailed explanation for this requirement would require a sophisticated derivation in quantum mechanics, and hence, it is omitted here. The consequence of the second requirement is that the direction of the electromagnetic field B_1 has to be perpendicular to the direction of the static magnetic field B_0 [1]. When both of the requirements are satisfied, an electron transition may happen, where the electron would absorb the electromagnetic energy and jumps from U_{lower} to U_{upper} .

III. ARCHITECTURE OF THE EPR SPECTROMETER

In this section, first, the architecture of the EPR spectrometer is presented. Second, the design strategies for individual components are discussed.

A. System Architecture

In this work, the proposed EPR spectrometer adopts an absorption-based architecture. As presented in Section II, chemical species with unpaired electrons absorb electromagnetic energy at a corresponding frequency ω when placed inside a static magnetic field B_0 . In practice, the absorption line would be broadened by effects such as thermal vibration and the interaction between the electron and the lattice. For example, for a fixed microwave frequency ω , the electromagnetic energy is absorbed across a range of magnetic field around B_0 . The absorption curve, which plots the relationship between the absorption level and the magnetic field under a constant microwave frequency ω , reveals some unique properties of chemical species. An EPR spectrometer is the equipment that is used to extract the absorption curve.

Fig. 2 shows the architecture of the proposed EPR spectrometer. It includes three major components, a static magnet, a resonator, and a single-chip electrical transceiver. In order to further reduce the cost and size of the proposed spectrometer, a

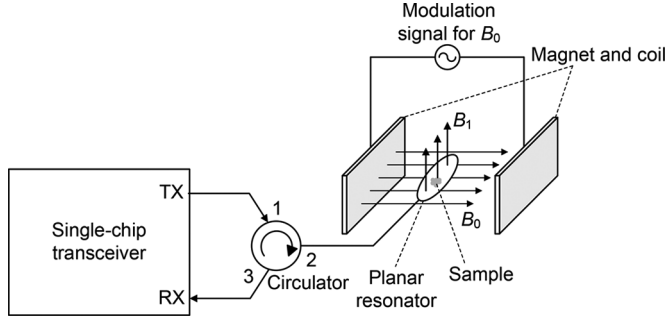


Fig. 2. Architecture of the proposed EPR spectrometer based on a fully integrated single-chip transceiver.

planar PCB-based resonator is utilized in this work, which is easy to fabricate, easy to operate, and has a small physical dimension. During the measurement, the transmitter delivers a microwave signal through the circulator to the resonator, which holds the sample. Inside the resonator, the microwave signal generates a strong electromagnetic field B_1 . The resonator is positioned such that B_1 is perpendicular to the static magnetic field B_0 . During the measurement, the frequency and power of the microwave signal is fixed, while the static magnetic field B_0 is swept. When EPR occurs, part of the electromagnetic energy is absorbed by the sample, altering the reflected microwave signal from the resonator. The change in the reflected power is monitored by the receiver to calculate the absorbed power.

In the proposed EPR spectrometer, the reflected microwave power is down-converted to baseband. In order to reduce the effects of low-frequency flicker noise and improve the sensitivity of the system, the static B_0 field is modulated and the reflected power is measured at the modulation frequency after down-conversion. Theoretically, a higher modulation frequency could reduce the flicker noise to a larger extent, but the modulation coil would require a much larger voltage to generate the same modulation field. To ease the burden of modulation voltage source and reduce safety concerns, the modulation frequency used in this work is 10 kHz. Due to the modulation of the static B_0 field, the absorption line of the sample is not observed directly. Instead, it is the first-order derivative of the absorption line that is measured.

B. Design Strategies

As derived in [3], the sensitivity of an EPR spectrometer, defined as the minimum number of spins that can be detected, is expressed as

$$\left(\frac{4k_B}{g^2\beta^2\mu_0} V_s T \right) \left(\frac{\Delta\omega}{\omega_0} \right) \left(\frac{1}{Q\eta} \right) \left(\frac{Fk_B T}{P} \right)^{1/2}. \quad (4)$$

Here, k_B is the Boltzmann constant. g is a material-dependent constant, known as the g factor. β is the orbital magnetic moment of an electron. μ_0 is the vacuum permeability. V_s is the sample volume. T is the temperature of the sample. ω_0 is the operational frequency of the EPR spectrometer. $\Delta\omega$ is the spectral linewidth of the sample, which is also a material-dependent constant. η and Q are the filling factor and the quality factor of the resonator, respectively. F is the noise factor of the receiver.

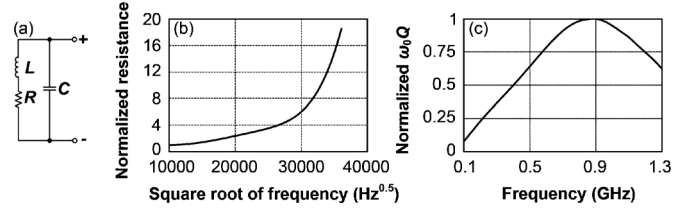


Fig. 3. (a) Lumped circuit model for the PCB inductor. (b) Simulated R versus the square root of frequency. (c) Simulated $\omega_0 Q$ versus frequency.

P is the microwave power sent to the sample. The equation assumes a bandwidth of 1 Hz for the data acquisition system.

To improve the sensitivity of the system, it is clear that the operating frequency ω_0 should be increased. On the other hand, for the PCB-based planar resonator used in this work, as the frequency increases, the quality factor Q may decrease due to the skin effect, substrate loss, and radiation effect, yielding a lower sensitivity. Therefore, maximizing ω_0 or Q alone does not guarantee the best sensitivity. Consequently, the product of $\omega_0 Q$ is used as a metric to investigate the optimal operating frequency. In this work, the resonator is fabricated on a 20-mil-thick Rogers 4350B PCB. The diameter of the inductor is set to be 8 mm, as it is expected to accommodate samples 5–6 mm wide. The inductor is modeled using an RLC circuit shown in Fig. 3(a). The resistance value is observed to increase with frequency, as shown in Fig. 3(b), which represents the increase in loss at higher frequencies. At low frequencies, the resistance is proportional to the square root of the frequency due to the skin effect. However, at higher frequencies, the resistance increases much faster due to other loss mechanisms, such as increased coupling to the ground, substrate loss, and radiation loss [18]. The quality factor of the inductor is then calculated using $\omega_0 L/R$. In Fig. 3(c), we present the simulation results of $\omega_0 Q$ versus different frequencies. As shown in this figure, $\omega_0 Q$ reaches a maximum value around 900 MHz.

We next determine the performance requirements for the fully integrated transceiver. According to (4), in order to obtain the highest sensitivity, the receiver noise figure (NF) should be minimized and the transmitter output power should be maximized. In practice, however, while the receiver NF is targeted at the lowest value, there are several nonidealities that restrict the largest power that can be delivered to the sample. First, (4) does not include the effects of sample saturation. It has been reported that as the incident microwave power exceeds the saturation power of the sample, the EPR signal would stop increasing or even decrease if the microwave power keeps rising. The amount of saturation power is usually determined by multiple factors, including the sample type, sample volume, temperature, etc. In EPR spectroscopy, the value of saturation power usually ranges from several hundred microwatts to tens of milliwatts [15]–[17]. Second, a portion of the transmitter power will leak to the receiver input due to the finite isolation of the circulator. This leakage power can be expressed as $P_{\text{out}} - I$, where P_{out} is the transmitter output power (in dBm) and I is the isolation value of the circulator (in dB). In order not to saturate the receiver and thus reduce the sensitivity, the leakage power is designed to be lower than the 1-dB compression power of the receiver ($P_{1\text{dB}}$). In practice, I is approximately 40 dB. As

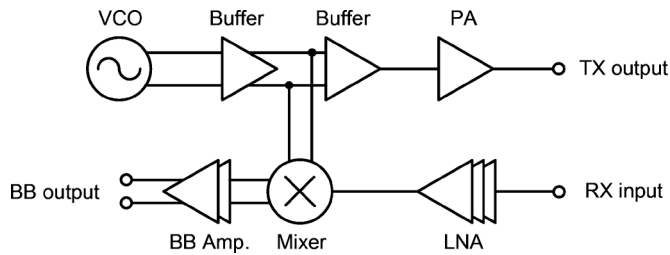


Fig. 4. Architecture of the single-chip transceiver.

discussed in Section IV, the receiver requires an RF gain of at least 30 dB before the mixer to minimize the receiver NF. The receiver $P_{1\text{dB}}$ is designed to be -35 dBm and P_{out} is targeted at $I + P_{1\text{dB}} = 5$ dBm.

IV. TRANSCEIVER DESIGN

Fig. 4 presents the architecture of the fully integrated transceiver reported in this work. In the transmitter path, a differential voltage-controlled oscillator (VCO) generates a microwave signal with tunable frequency. The differential signal is amplified by a buffer following the VCO. It is then converted into a single-ended signal through a differential-to-single-ended converter. The single-ended signal is delivered to the 50- Ω resonator through a power amplifier (PA). In the receiver path, a single-ended low-noise amplifier (LNA) amplifies the reflected signal from the resonator. The amplified signal is then down-converted to baseband through a differential mixer. The local oscillator (LO) signal of the mixer is provided from the same VCO in the transmitter path. The down-converted signal is further amplified by the baseband amplifier and delivered to off-chip equipment for processing.

One important task of the design is to determine the gain allocation in the receiver. In wireless communication, many receivers provide a strong amplification at the baseband with much smaller gain at the RF [18]. Such receivers usually consume less power, ease the design of the LNA, and impose minimal impact on the receiver NF. In this work, unfortunately, such design strategies cannot be adopted. As stated in Section III, the baseband frequency in this design is located at 10 kHz. At such low frequency, the flicker noise from the mixer and baseband amplifier may dominate the receiver NF if insufficient voltage amplification before down-conversion is used. In Fig. 5, the simulated NF of the receiver is reported under different LNA gain values, assuming that each block is matched to 50 Ω and the LNA NF is 3 dB. The combined NF of the mixer and baseband amplifier is assumed to be 20 dB, which is a typical value at 10-kHz IF. As shown in the figure, the NF of the receiver decreases drastically as the LNA gain increases, and it saturates at 3 dB as the LNA gain reaches 30 dB. As a result, to minimize the receiver NF, the LNA gain is targeted at 30 dB.

Next, the circuit implementation details for several important blocks are reported.

A. 900-MHz VCO

In this work, the microwave signal is generated using a VCO. The choice of a VCO instead of an oscillator with fixed frequency is to compensate for the effects of process variation,

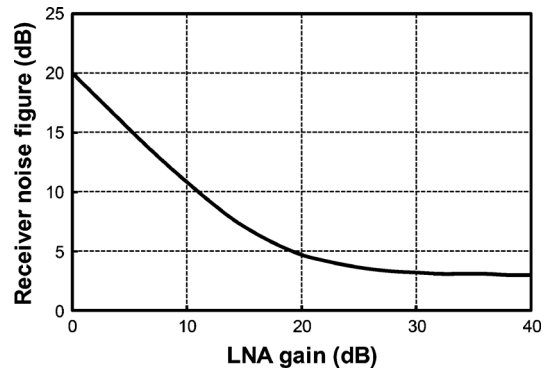


Fig. 5. Simulated NF of the receiver under different LNA gain values.

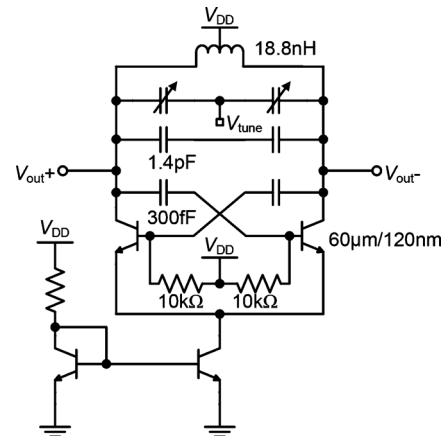


Fig. 6. Schematic of the VCO.

which may alter the optimal operational frequency of on-chip amplifiers, as well as the resonance frequency of the resonator. Fig. 6 shows the schematic of the VCO, which adopts a differential cross-coupled structure. A symmetric inductor is used in this work to provide a reactance of 122 Ω at 900 MHz. The quality factor Q of the inductor is 10.2 at this frequency. The varactors of the VCO are implemented using reverse-biased diodes. The capacitance versus the reverse bias of the varactors is simulated. It is observed that the capacitance decreases by 60% as the reverse bias increases from 0 to 3 V.

B. 900-MHz PA

As described in Section IV-B, the maximum output power of the PA is targeted at 5 dBm. Fig. 7 shows the schematic of the PA. It adopts a single-ended cascode structure to improve the reverse isolation, and hence, the stability. The input of the PA is co-designed with the preceding buffer to maximize the input voltage. The output of the PA is matched to 50 Ω using on-chip capacitors and inductors. The load network is tuned to enable maximum output power at 900 MHz. To improve the stability of the PA, a capacitor is used at the base of M_2 to reduce the high-frequency voltage swing.

C. LNA

As described previously, the LNA gain is targeted at 30 dB. The schematic for the LNA is presented in Fig. 8, which incorporates a three-stage design. The input of the LNA is matched to 50 Ω . An ac-coupling capacitor is used between different stages so that each stage can be biased separately. As the LNA has a

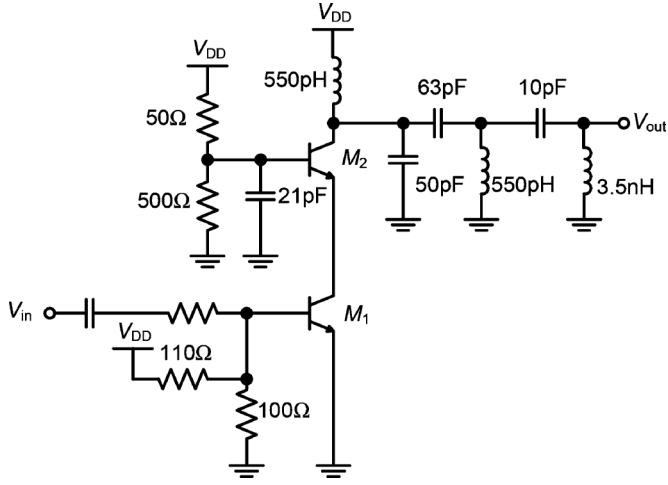


Fig. 7. Schematic of the PA.

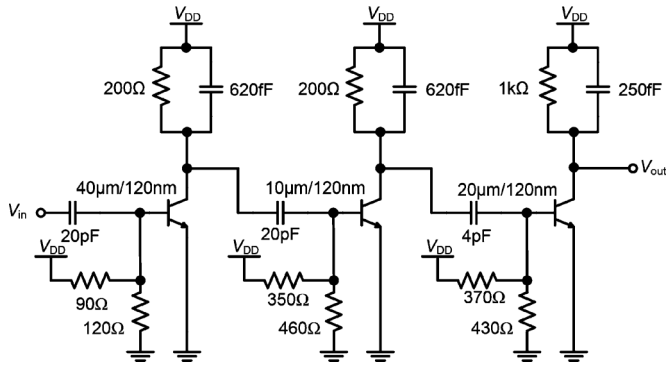


Fig. 8. Schematic of the LNA.

large voltage gain, extra care must be taken to prevent oscillation. As shown in the figure, capacitors are added at the load to reduce the bandwidth of the LNA. This improves high-frequency stability, as well as noise performance. The simulated NF of the LNA versus frequency is presented in Fig. 9. It is observed that the NF is 3.89 dB at 900 MHz.

D. Mixer and Baseband Amplifiers

In this work, we adopt a double-balanced active mixer with a Gilbert cell structure. The mixer is co-designed with the last stage of the LNA to maximize the input voltage. The load of the mixer is an RC network, which behaves as a low-pass filter. Note that the active mixer is adopted due to its large gain and high robustness. If a passive mixer is used, the NF of the receiver would further improve due to the low flicker noise. The baseband amplifier incorporates a two-stage design. The first stage is a source follower, which serves to shift the dc components of the signal to 0.85 V. The second stage of the baseband amplifier adopts a common-source architecture. The output of the amplifier is matched to 50 Ω .

V. RESONATOR DESIGN

The resonator is a crucial component in the EPR spectrometer. Since the goal of this work is to build an EPR spectrometer with low cost and small physical dimensions, a PCB-based planar resonator is used in this work, which enjoys the advantages of easy fabrication and ease of use. However, if the sensitivity is of a higher concern, the planar resonator can always

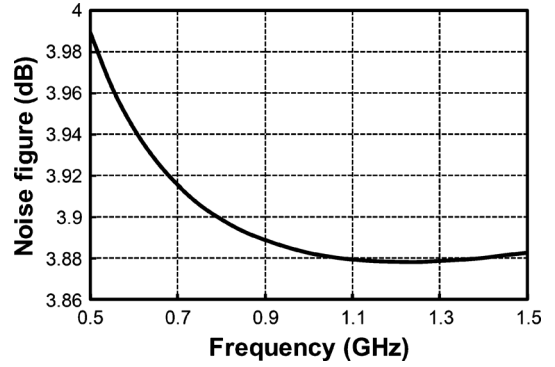


Fig. 9. Simulated NF of the LNA.

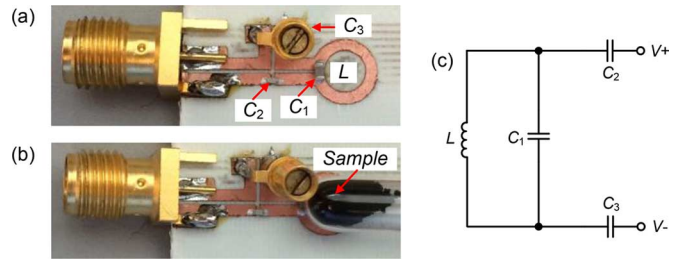


Fig. 10. (a) Image of the fabricated resonator. (b) Image of the resonator with loaded sample. (c) Equivalent lumped circuit model of the resonator.

be replaced by a 3-D resonator that is used in commercial EPR spectrometers and has a higher quality factor.

The design of the proposed planar resonator is presented in Fig. 10(a). The PCB structure is fabricated in-house using a 20-mil-thick Rogers 4350B board. The resonator includes a PCB-based inductor and three capacitors. During the EPR measurement, the samples are placed at the center of the inductor loop where the magnetic field is the strongest. The position of the sample is illustrated in Fig. 10(b). Thanks to the planar geometry, the resonator can be easily used in *in vivo* measurement in future. Moreover, unlike the high- Q 3-D resonator, the quality factor of the planar resonator will not be significantly impacted when measuring lossy samples. The equivalent lumped circuit model of the resonator is shown in Fig. 10(c). The inductor provides an inductance of 4.1 nH at 900 MHz in simulation, with a quality factor of 72. The capacitor C_1 provides a capacitance of 6.8 pF, resonating with the inductor at 965-MHz frequency. The capacitors C_2 and C_3 serve to match the input impedance of the resonator to 50 Ω . During the design, C_2 is fixed at 1 pF while C_3 is implemented using a tunable capacitor to compensate for process variation during the fabrication. The reflection coefficient of the fabricated resonator without any loaded sample is measured. As presented in Fig. 11, the resonator has a resonance frequency of 913 MHz with a quality factor of approximately 30.

VI. MEASUREMENT RESULTS

In this section, we first describe the measurement results of the integrated transceiver. We next present the measured sample absorption curve using the reported EPR spectrometer.

A. Transceiver Measurement Results

The fully integrated transceiver is implemented using IBM 0.13- μm SiGe BiCMOS process technology. The micrograph

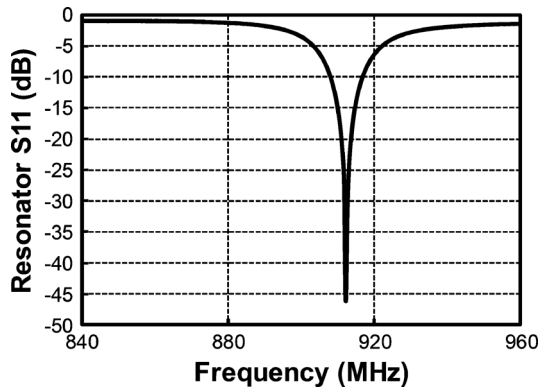


Fig. 11. Measured reflection coefficient of the resonator.

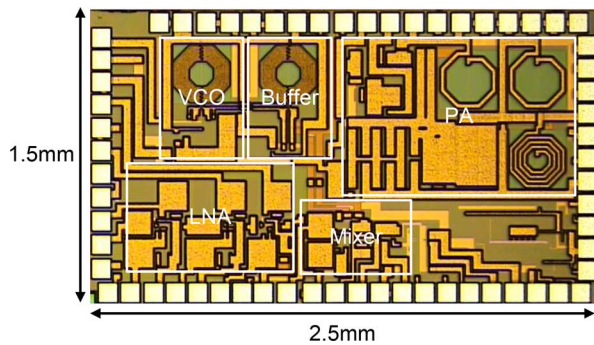


Fig. 12. Micrograph of the fully integrated transceiver chip.

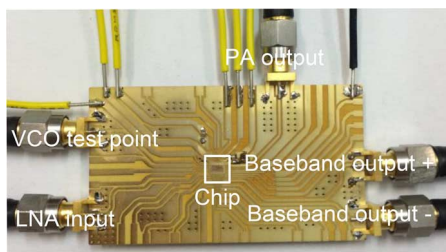


Fig. 13. PCB assembly for chip testing.

of the fabricated chip is presented in Fig. 12. It occupies an area of 1.5 mm by 2.5 mm. Important blocks of the transceiver are labeled in the figure. For testing purposes, the chip is wirebonded onto a PCB, as shown in Fig. 13.

Fig. 14 plots the measured VCO frequency versus the tuning voltage at a supply voltage of 1.5 V. The VCO can be tuned from 885 to 979 MHz with a tuning range of 10.2%. It has a measured phase noise of -118 dBc/Hz at 1-MHz frequency offset.

Fig. 15 plots the transmitter output power versus frequency. It is observed that the transmitter can deliver a maximum power of 5.2 dBm at 885 MHz. The appearance of the maximum power at 885 MHz instead of at the center frequency is most likely due to the off-tune of the buffer and/or the PA in the transmitter path.

Fig. 16 plots the receiver conversion gain versus the input RF frequency. During the measurement, the VCO frequency is fixed at 935 MHz. The input of the on-chip LNA is excited by an RF source. The frequency of the RF source is varied, and the corresponding down-converted signal at the output of the on-chip baseband amplifier is measured. The measured receiver conversion gain is 40.5 dB with a 3-dB bandwidth of 25 MHz. The measurement of the receiver conversion gain versus the input

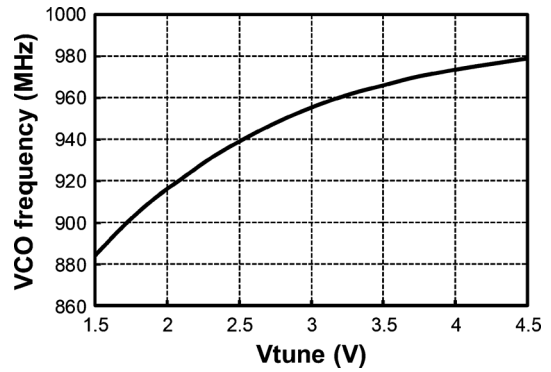


Fig. 14. Measured tuning range of the VCO.

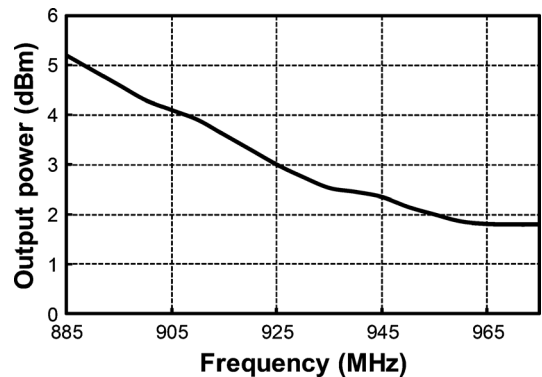


Fig. 15. Measured output power of the transmitter versus the frequency.

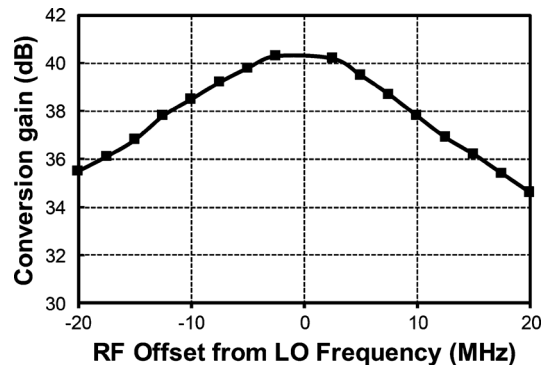


Fig. 16. Measured conversion gain of the receiver versus the RF frequency. The LO frequency is 935 MHz.

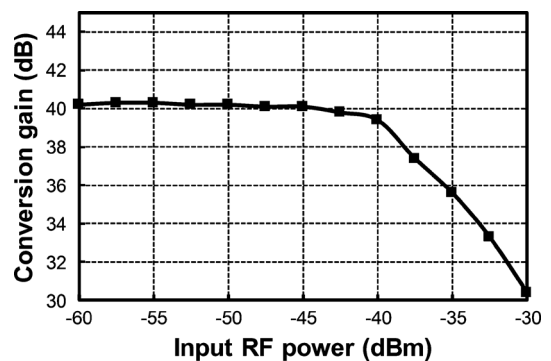


Fig. 17. Measured conversion gain of the receiver versus the input RF power.

RF power is presented in Fig. 17. The measured input-referred $P_{1\text{dB}}$ is -40 dBm. This is approximately 5 dB lower than the designed value, but it can be compensated by using a circulator with a higher isolation value.

B. EPR Spectrometer Characterization

The proposed EPR spectrometer based on the fully integrated transceiver and a PCB-based planar resonator is assembled and tested. A circulator with a maximum isolation value of 45 dB is used in this work. As the maximum transmitter power is 5 dBm and the receiver $P_{1\text{ dB}}$ is -40 dBm, the isolation value of the circulator is high enough so that the receiver gain is not significantly affected. In order to minimize the sensitivity degradation resulting from the VCO phase noise, the relative path delay between the TX leakage and the LO of the mixer is kept small. As shown in [19], the effect of phase noise would quickly vanish as the relative path delay is reduced because the same VCO is used for the TX and the LO of the RX. It should be noted that although currently fabricated on a separate PCB, the planar resonator can be easily fabricated on the same PCB that holds the fully integrated transceiver. With the adoption of a surface-mount circulator and a rare-earth magnet, the entire spectrometer will be as small as the size of a human hand.

In this work, three different samples are measured using the proposed EPR spectrometer to demonstrate its functionality. Due to the placement of samples onto the resonator, the resonance frequency of the resonator varies slightly. Therefore, each time a different sample is placed, the resonance frequency of the resonator is re-measured and the VCO frequency in the transmitter is adjusted accordingly. The measurement of the resonance frequency can be easily achieved without changing the setup by inserting a power coupler between the circulator and the receiver. As introduced in Section VI-A, the static magnetic field is modulated in this work to avoid the low-frequency flicker noise and improve the sensitivity of the system. This is achieved by exciting a custom-fabricated coil with a 10-kHz signal to generate the modulation magnetic field. The modulation field is measured to be 1.2 G at the resonator location.

We first measure the absorption line of a 4-mg DPPH powder sample. The frequency of the incident microwave signal is fixed at 914 MHz. The static magnetic field is swept from 310 to 322 G. The measured response curve of the DPPH sample is presented in Fig. 18. Due to the modulation of the magnetic field, the measured response curve is the first-order derivative of the absorption line, which takes a Lorentzian shape. The linewidth of the sample, defined as the separation between the positive and negative peaks of the curve, is 3 G. This matches well with previously published experimental results. The difference between the magnitudes of the two peaks is possibly due to the superposition of the dispersion curve on the absorption curve. This can be potentially improved by matching the time delay of the RF and LO paths in the active mixer.

We next measure the absorption line of a 61-mg Fe_2O_3 nanoparticle sample, the average particle size (APS) of which is 20 nm. The frequency of the incident microwave signal is fixed at 900 MHz. The static magnetic field is swept from 0 to 1000 G. The measured response curve of the Fe_2O_3 sample is presented in Fig. 19. The separation between the positive and negative peaks of the curve is 500 G.

We finally report the measured absorption line of a 63-mg Fe_3O_4 nanoparticle sample, the APS of which is 15–20 nm. The frequency of the incident microwave signal is 902 MHz. The

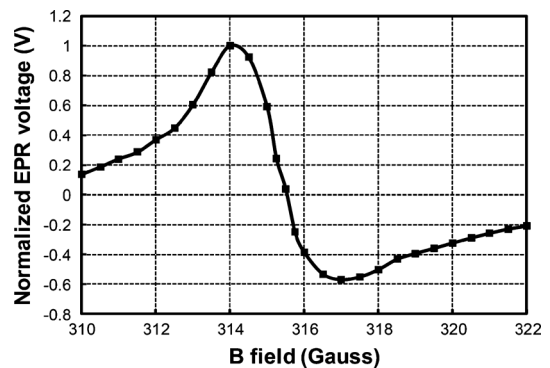


Fig. 18. Measured EPR signal voltage of DPPH.

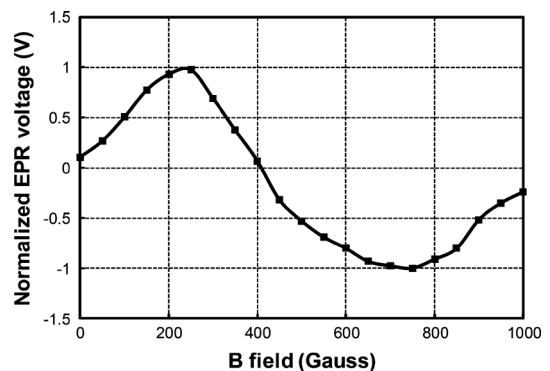


Fig. 19. Measured EPR signal voltage of Fe_2O_3 .

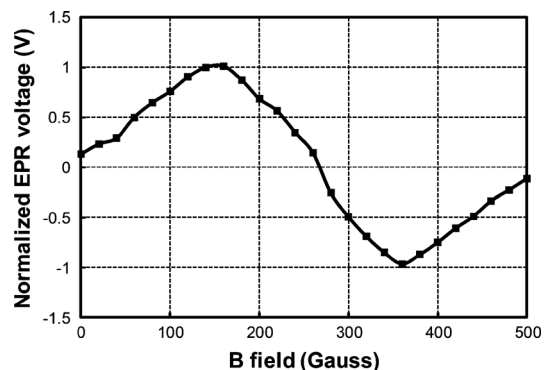


Fig. 20. Measured EPR signal voltage of Fe_3O_4 .

static magnetic field is swept from 0 to 500 G. The measured response curve of the Fe_3O_4 sample is presented in Fig. 20. The separation between the positive and negative peaks of the curve is 200 G.

From the measurement results presented above, it is clear that the proposed EPR spectrometer can measure the EPR response from various samples with different line shapes. This demonstrates the functionality of the spectrometer and the feasibility of our design. As shown in Table I, compared to previous works that tried to integrate the electronics of the EPR spectrometer, the proposed work represents the first absorption-based fully integrated single-chip transceiver. It achieves a significantly higher integration level and is more suitable in field or *in vivo* measurement of relatively large samples.

We now estimate the sensitivity of the proposed EPR spectrometer. It is known that DPPH contains 1.53×10^{21} unpaired electrons per gram [20]. Considering that 4 mg of DPPH is used in the experiment and the signal-to-noise ratio is approximately

TABLE I
COMPARISON WITH PREVIOUS INTEGRATED CIRCUITS FOR EPR SPECTROMETERS

	[12]	[13]	This work
System architecture	Frequency-shift based	Frequency-shift based	Absorption based
Frequency	~27 GHz	~9 GHz	~900 MHz
On-chip blocks	Fixed-frequency oscillator and divider	VCO, mixer, and divider	Complete transceiver including VCO, power amplifier, LNA, mixer, and baseband amplifier
Active off-chip components required? ¹	Yes. (Power amplifier, mixer, multiple operational amplifiers, and phase-locked loop)	Yes. (Power amplifier, mixer, multiple operational amplifiers, and phase-locked loop)	No.
Effective sample volume ² (order)	10 ⁻³ mm ³	10 ⁻³ mm ³	10 mm ³
Process	0.13 μm CMOS	0.35 μm CMOS	0.13 μm BiCMOS
Area	1 mm ²	1 mm ²	3.75 mm ²

1. Power supply and data acquisition system are not counted here.

2. The samples in [12] and [13] are placed on an on-chip inductor. The samples in this work are placed on an off-chip resonator.

10 without averaging at 60-s measurement time, the sensitivity of the spectrometer is estimated as $1.53 \times 10^{21} \times 0.004/10 = 6 \times 10^{17}$ spin. Since the EPR response of a sample is proportional to its linewidth, the sensitivity can be further normalized by the linewidth of DPPH to 2×10^{17} spin/G. As a comparison, the sensitivity of existing EPR spectrometers that are costly and bulky is usually below 10^{14} spin/G (e.g., a Fizepr EPR VIGT.421400.012 spectrometer, an Adani EPR CMS8400 spectrometer, and [21]). The high sensitivity of existing spectrometers mostly result from the adoption of a high- Q resonator with a larger filling factor (2–3 orders of magnitude higher than in this work) and a higher operational frequency (typically more than one order of magnitude higher than in this work). If the sensitivity is of a higher concern, instead of the cost and physical size, the PCB-based planar resonator used in this work can always be replaced by a high- Q resonator. This will bring the sensitivity of the proposed EPR spectrometer to be comparable to that of existing products, while the cost and physical size are still much lower due to the adoption of a fully integrated transceiver.

The sensitivity obtained during the measurement for the proposed spectrometer is also compared with the theoretical value calculated using (4). The parameters related to the spectrometer in the equation, such as P and F , are substituted by the measured values of the proposed system. The theoretical minimum number of spins that can be detected is calculated to be on the order of 10^{15} spin for DPPH. It is two orders of magnitude better than the sensitivity in measurement, which is a 6×10^{17} spin. We believe this difference can be attributed to multiple reasons, including: 1) the theoretical sensitivity does not take into account of the sample saturation behavior; 2) the noise contribution from the data acquisition system; and 3) other noise sources such as the phase noise of the oscillator. As a comparison, the difference between the theoretical and measured sensitivity for commercial EPR spectrometers is usually under one order of magnitude, which is possibly due to the superior data acquisition system and oscillator.

VII. CONCLUSION

In this paper, we report the first absorption-based EPR spectrometer by integrating the entire transceiver on a single silicon chip. The reported work can significantly reduce the cost and physical dimensions of the existing EPR spectrometers. In order

to demonstrate the feasibility and functionality of the EPR transceiver, a complete spectrometer is assembled using the fully integrated single-chip transceiver and a custom resonator. The spectrometer is then used to successfully measure the EPR spectrum of various samples such as DPPH, Fe₂O₃, and Fe₃O₄.

REFERENCES

- [1] J. A. Weil and J. R. Bolton, *Electron Paramagnetic Resonance: Elementary Theory and Practical Applications*. New York, NY, USA: Wiley, 2006.
- [2] D. Canet, *Electron Paramagnetic Resonance: Elementary Theory and Practical Applications*. New York, NY, USA: Wiley, 1996.
- [3] J. C. P. Poole and H. A. Farach, *Handbook of Electron Spin Resonance*. New York, NY, USA: Springer, 1999, vol. 2.
- [4] S. Velan, R. Spencer, J. Zweier, and P. Kuppusamy, "Electron paramagnetic resonance oxygen mapping (EPRM): Direct visualization of oxygen concentration in tissue," *Magn. Reson. Med.*, vol. 43, pp. 804–809, 2000.
- [5] J. Jiang, T. Nakashima, K. J. Liu, F. Goda, T. Shima, and H. M. Swartz, "Measurement of PO₂ in liver using EPR oximetry," *J. Appl. Physiol.*, vol. 80, pp. 552–558, 1996.
- [6] J. Matsumoto *et al.*, "Absolute oxygen tension (pO₂) in murine fatty and muscle tissue as determined by EPR," *Magn. Reson. Med.*, vol. 54, pp. 1530–1535, 2005.
- [7] Y. Lee and J. Corbett, "EPR studies of defects in electron-irradiated silicon: A triplet state of vacancy-oxygen complexes," *Phys. Rev. B, Condens. Matter*, vol. 13, pp. 2653–2666, 1976.
- [8] J. Isoya, T. Umeda, N. Mizuochi, N. Son, E. Janzén, and T. Ohshima, "EPR identification of intrinsic defects in SiC," *Phys. Status Solidi (b)*, vol. 245, pp. 1298–1314, 2008.
- [9] K. Vanheusden, C. H. Seager, W. L. Warren, D. R. Tallant, and J. A. Voigt, "Correlation between photoluminescence and oxygen vacancies in ZnO phosphors," *Appl. Phys. Lett.*, vol. 68, pp. 403–405, 1996.
- [10] C. Benelli and D. Gatteschi, "Magnetism of lanthanides in molecular materials with transition-metal ions and organic radicals," *Chem. Rev.*, vol. 102, pp. 2369–2387, 2002.
- [11] I. Salikhov *et al.*, "EPR spectrometer for clinical applications," *Magn. Reson. Med.*, vol. 54, pp. 1317–1320, 2005.
- [12] J. Anders, A. Angerhofer, and G. Boero, "K-band single-chip electron spin resonance detector," *J. Magn. Reson.*, no. 217, pp. 19–26, 2012.
- [13] T. Yalcin and G. Boero, "Single-chip detector for electron spin resonance spectroscopy," *Rev. Sci. Instrum.*, no. 79, 2008, Art. ID 094105.
- [14] X. Yang, P. Seifi, and A. Babakhani, "A single-chip dual-mode CW/pulse electron paramagnetic resonance spectrometer in 0.13 μm SiGe BiCMOS," in *IEEE MTT-S Int. Microw. Symp. Dig.*, 2013, pp. 1–4.
- [15] N. J. Malmberg and J. J. Falke, "Use of EPR power saturation to analyze the membrane-docking geometries of peripheral proteins: Applications to C2 domains," *Annu. Rev. Biophys. Biomol. Struct.*, vol. 34, pp. 71–90, 2005.
- [16] N. D. Yordanova, K. Aleksieva, and I. Mansour, "Improvement of the EPR detection of irradiated dry plants using microwave saturation and thermal treatment," *Radiat. Phys. Chem.*, vol. 73, pp. 55–60, 2005.
- [17] B. Sanyal, S. P. Chawla, and A. Sharma, "An improved method to identify irradiated rice by EPR spectroscopy and thermoluminescence measurements," *Food Chem.*, vol. 116, pp. 526–534, 2009.

- [18] B. Razavi, *RF Microelectronics*. Englewood Cliffs, NJ, USA: Prentice-Hall, 1998.
- [19] A. Sahai, G. Patel, C. Dick, and A. Sabharwal, "On the impact of phase noise on active cancellation in wireless full-duplex," *IEEE Trans. Veh. Technol.*, vol. 62, no. 9, pp. 4494–4510, Nov. 2013.
- [20] A. Hayes, *Principles and Methods of Toxicology*. Boca Raton, FL, USA: CRC, 2007.
- [21] F. Simon and F. Muranyi, "ESR spectrometer with a loop-gap resonator for CW and time resolved studies in a superconducting magnet," *J. Magn. Reson.*, vol. 173, pp. 288–295, 2005.



Xuebei Yang (S'09) received the B.S. degree in microelectronics from Tsinghua University, Beijing, China, in 2008, the M.S. degree in electrical and computer engineering from Rice University, Houston, TX, USA, in 2010, and is currently working toward the Ph.D. degree at Rice University.

His research interest includes analog/RF/millimeter-wave circuits and CMOS-based photonics.

Mr. Yang was the recipient of the IEEE Microwave Theory and Techniques Society (IEEE MTT-S) Graduate Fellowship for medical applications and

the Chinese Government National Award for Outstanding Self-financed Students Abroad, both in 2015.



Aydin Babakhani (M'08) received the B.S. degree in electrical engineering from the Sharif University of Technology, Tehran, Iran, in 2003, and the M.S. and Ph.D. degrees in electrical engineering from the California Institute of Technology, Pasadena, CA, USA, in 2005 and 2008, respectively.

He is currently an Assistant Professor with the Electrical and Computer Engineering Department, Rice University, Houston, TX, USA, and the Director of the Rice Integrated Systems and Circuits Laboratory. In 2009, he was a Postdoctoral Scholar with the California Institute of Technology. In 2010, he was a Research Scientist with the IBM T. J. Watson Research Center.

Dr. Babakhani was the vice chair of the IEEE Microwave Theory and Techniques Society (IEEE MTT-S) Metro LA/SFV Joint Sections, MTT-S Chapter 17.1 from 2006 to 2008. He was the recipient of the Best Paper Award of the IEEE RWS Symposium (2015), the Best Paper Award of the IEEE MTT-S International Microwave Symposium (IMS) (2014), an Innovation Qward from Northrop Grumman (2014), a Defense Advanced Research Projects Agency (DARPA) Young Faculty Award (YFA) (2012), the California Institute of Technology Electrical Engineering Department's Charles Wilts Best Ph.D. Thesis Prize for his work on near-field direct antenna modulation (NFDAM) (2008), the Microwave Graduate Fellowship (2007), the Grand Prize in the Stanford–Berkeley–Caltech Innovators Challenge (2006), the Analog Devices Inc. Outstanding Student Designer Award (2005), the California Institute of Technology Special Institute Fellowship (2003), and the Atwood Fellowship (2003). He was also the Gold Medal recipient of the National Physics Competition (1998), and the Gold Medal of the 30th International Physics Olympiad (1999), Padova, Italy.